Title

Laboratory and numerical modeling of the formation of superfog from wildland fires

Authors

Bartolome, Christian
Princevac, Marko
Weise, David R
et al.

Publication Date

2019-06-01

DOI

10.1016/j.firesaf.2019.04.009

Peer reviewed

Fire Safety Journal 106 (2019) 94–104

Contents lists available at ScienceDirect

Fire Safety Journal

journal homepage: www.elsevier.com/locate/firesaf

Laboratory and numerical modeling of the formation of superfog from wildland fires☆

Christian Bartolome[a], Marko Princevac[a,*], David R. Weise[b], Shankar Mahalingam[c], Masoud Ghasemian[a], Akula Venkatram[a], Henry Vu[a], Guillermo Aguilar[a]

[a] Department of Mechanical Engineering, University of California, Riverside, CA, USA
[b] PSW Research Station, USDA Forest Service, Riverside, CA, USA
[c] Department of Mechanical and Aerospace Engineering, The University of Alabama in Huntsville, AL, USA

ARTICLE INFO

Keywords:
Superfog
Visibility
Liquid water content
Prescribed fire
Cloud condensation nuclei

ABSTRACT

Smoke from human-induced fires such as prescribed fires can occasionally cause significant reduction in visibility on highways in the southern United States. Visibility reduction to less than 3 m has been termed "superfog" and environmental conditions that lead to its formation have been proposed previously. Accurate characterization and prediction of precursor conditions for superfog is needed to prevent dangerous low visibility situations when planning prescribed fires. It is hypothesized that extremely hygroscopic cloud condensation nuclei from the smoldering phase of a fire can produce a large number of droplets smaller in size than in naturally occurring fog. This large number of small droplets can produce superfog conditions with relatively low liquid water content. A thermodynamics-based model for fog formation was developed. Laboratory generated superfog measured by a Phase Doppler Particle Analyzer determined that mean droplet radius was 1.5 μm and the size distribution could be modeled with a lognormal distribution. Experiments in an environmentally-conditioned wind tunnel using longleaf pine (*Pinus palustris* Mill.) needle fuel beds provided visibility, heat flux, temperature, humidity, and particle data for model validation. Numerical modeling was used to approximate the growth of a superfog boundary-layer with liquid water content values of $2\,g\,m^{-3}$ or greater. The model successfully predicted previous superfog events.

1. Introduction

Prescribed fires are a common tool used by wildland managers to reduce hazardous fuel accumulations, enhance wildlife habitat, and stimulate plant regeneration [1]. In 2014, an estimated 11.7 million acres were treated with prescribed fire in the United States; 6.19 million acres were treated for forestry activities in the southern U.S. alone [2]. Smoke management for prescribed burning has long been a concern because of the potential impacts on air quality and visibility [3]. In rare cases a combination of smoke and fog has crossed over major roadways leading to visibility less than 3 m, a condition known as superfog [4–7], resulting in traffic accidents. In January 9, 2008, on the I-4 in Polk County Florida, a superfog event resulting from a nearby prescribed fire caused a 70 car pileup which resulted in 5 fatalities and 38 injuries. In 2011 wildfires caused low visibility events resulting in numerous highway closures over a 3 month period at the Great Dismal Swamp National Wildlife Refuge. There were isolated vehicular accidents caused by low visibility despite the best efforts of highway management. In December 2011 marsh wildfire smoke caused superfog conditions leading to a major car pileup on the I-10 in New Orleans, LA. The accident caused 2 deaths and 61 injuries. In January 2012 a superfog event formed from a nearby wildfire on the I-75 near Gainesville, FL. The pileup included 7 semi-trucks and 12 cars. This event claimed 10 lives and left 21 injured.

Superfog is hypothesized to form during the smoldering phase of a wildland fire in the night hours [8]. The smoldering phase releases water vapor and particulates that act as cloud condensation nuclei (CCN) [8–11]. Mixing between the cool ambient air, hot water vapor, and CCN leads to vapor condensation into droplets. The presence of numerous droplets in air causes extreme light scattering, thereby reducing visibility. Visibility is strongly dependent on the size distribution of particles and number concentration of droplets.

This study aims to provide the first order understanding of superfog formation through combination of boundary layer development,

☆ This manuscript was prepared, in part, by a U.S. Government employee on official time, is not subject to copyright and is in the public domain.

* Corresponding author. Bourns A359, Department of Mechanical Engineering, University of California, Riverside, 900 University Ave, Riverside, CA, 92521, USA.
E-mail address: marko@engr.ucr.edu (M. Princevac).

https://doi.org/10.1016/j.firesaf.2019.04.009
Received 1 September 2018; Received in revised form 13 March 2019; Accepted 18 April 2019
Available online 23 April 2019
0379-7112/

environmental conditions and smoke. In this paper, we present the development of a coupled thermodynamics and physics-based model of superfog formation and the supporting laboratory experiments used to parameterize and evaluate the model. The theoretical background is presented in Section 2 followed by a description of experimental setups in Section 3. Comparison of the experimental data with the theoretical model is presented in Section 4, and the primary findings of this work are summarized in Section 5.

2. Theoretical background

A major factor in cloud, fog, and superfog formation is the amount of available liquid water. There are several mechanisms that lead to fog formation: 1) radiation fog [12], 2) advection fog [13], 3) upslope fog [14], 4) ice fog [15], 5) freezing fog [16], and 6) steam fog [17]. The superfog phenomenon is most akin to steam fog. In a steam fog, cold air masses flow over a water body leading to condensation of water vapor. In case of superfog, the water body is replaced by smoldering fuel bed which contributes heated water vapor by combustion and pyrolysis reactions, evaporation of water from wet wildland fuels, and vaporization of soil moisture. This released moisture interacts subsequently with the ambient atmospheric moisture. Maximum water vapor in the air is exponentially related to temperature based on the Clausius-Clayperon relation [18]. If there is excess water over the saturation water vapor pressure, liquid water condenses into micro size aerosols. The liquid water content depends strongly on the final temperature and saturation vapor pressure of the mixture.

2.1. Thermodynamic model

A mass balance based on thermodynamic equilibrium of water vapor resulting from perfect mixing of a warm, humid air mass with a cool, dry air mass yields:

$$w_3 = \frac{m_1 w_1 + m_2 w_2}{m_1 + m_2} = \frac{m_s w_s + m_a w_a}{m_s + m_a} \tag{1}$$

where w_i is the mixing ratio (*i.e.* the mass of water vapor per unit of dry air mass) (g kg^{-1}) and m_i is the mass of air (i=1 – warm and humid, 2 – cool and dry, 3 – mixture of 1 and 2). Indices s and a correspond to vapor released by smoldering and ambient vapor, respectively. An initial estimate of temperature is made through a weighted average.

$$T_3 = \frac{m_1 T_1 + m_2 T_2}{m_1 + m_2} = \frac{m_s T_s + m_a T_a}{m_s + m_a} \tag{2}$$

where T_i is the temperature at state 1, 2 or 3. Applied to fog formation in the presence of smoke, state 1 represents smoke plume conditions (T_s, m_s) and state 2 denotes ambient conditions (T_a, m_a). The final temperature, T_f, is obtained via energy balance as

$$T_f = T_3 + \Delta T \tag{3}$$

where ΔT is temperature change due to latent heat of condensation calculated as:

$$\Delta T = (w_3 - w_{sat})\frac{h_{fg}}{C_p} \tag{4}$$

where w_{sat} is the saturation mixing ratio, h_{fg} is the latent heat of condensation for water vapor, and C_p is the specific heat capacity of water. Eq. (4) is cast in a form suitable for iterative solution as:

$$f(T_f) = T_f - T_3 - (w_3 - w_{sat})\frac{h_{fg}}{C_p} = 0 \tag{5}$$

Noting that the saturation mixing ratio is a function of temperature, but the latent energy and heat capacity do not depend on temperature, the derivative function is obtained as follow:

$$f'(T_f) = 1 + \frac{h_{fg}}{C_p}\frac{d}{dT}(w_{sat}) \tag{6}$$

Lowe's [19] polynomial function is adopted to calculate the vapor pressure of water as a function of temperature:

$$p_{sat}(T) = a_0 + a_1 T + a_2 T^2 + a_3 T^3 + a_4 T^4 + a_5 T^5 + a_6 T^6 \tag{7}$$

Here p_{sat} is the saturation vapor pressure in millibars, T is the temperature in degree Celsius, and $a_0 - a_6$ are experimentally determined fit coefficients available in Lowe's [19].

The saturation vapor pressure is linked to the saturation mixing ratio as follow:

$$w_{sat} = \frac{0.622 \times p_{sat}}{1013.25 - p_{sat}} \tag{8}$$

The Newton Raphson iterative method is used to solve for the final temperature.

$$T_f^{i+1} = T_f^i - \frac{f(T_f^i)}{f'(T_f^i)} \tag{9}$$

The excess liquid mixing ratio, w_l, is expressed as:

$$w_l = w_3 - w_{sat}(T_f) \tag{10}$$

Excess liquid mixing ratio can be related to the liquid water content through

$$C_{H_2O} = w_l \rho_a \tag{11}$$

where ρ_a is the density of ambient air.

2.2. Relationship of liquid water content (C_{H_2O}) and visibility

Although eq. (11) provides the predicted liquid water content based on the thermodynamic equilibrium model, it cannot be related directly to the resulting visibility. Liquid water content and extinction coefficient are coupled by the distribution and size of droplets of water in the produced fog. Liquid water content can be calculated as [20].

$$C_{H_2O} = \int_{r_1}^{r_2} \frac{4\pi}{3} r^3 \rho_l n(r) dr \tag{12}$$

where r is the radius of droplet, r_1 and r_2 are the lower and upper droplet size limits, $n(r)$ is the probability density function for the droplet size distribution, and ρ_l is the density of water. The extinction coefficient β [14,21] is calculated as

$$\beta = \int_{r_1}^{r_2} \pi Q_e(r, \lambda) n(r) r^2 dr \tag{13}$$

where Q_e is the extinction efficiency calculated via Mie theory and is a strong function of droplet radius and the wavelength of light, λ. In Fig. 1 a plot of the extinction efficiency is presented for four wavelengths. We see that droplets with radii less than 1 μm can have extinction efficiencies near 4. For droplets with radii larger than 2 μm, the extinction efficiency oscillates around a value of 2.

Finally, visibility is related to the extinction coefficient as [22].

$$V = -\frac{\ln(\varepsilon)}{\beta} \tag{14}$$

where ε is the contrast limit commonly accepted as 0.02.

Both liquid water content and visibility are strongly dependent on the size distribution and number concentrations of the droplets formed. We modelled the probability density distribution of aerosol droplet size in the atmosphere with the lognormal distribution [23–26].

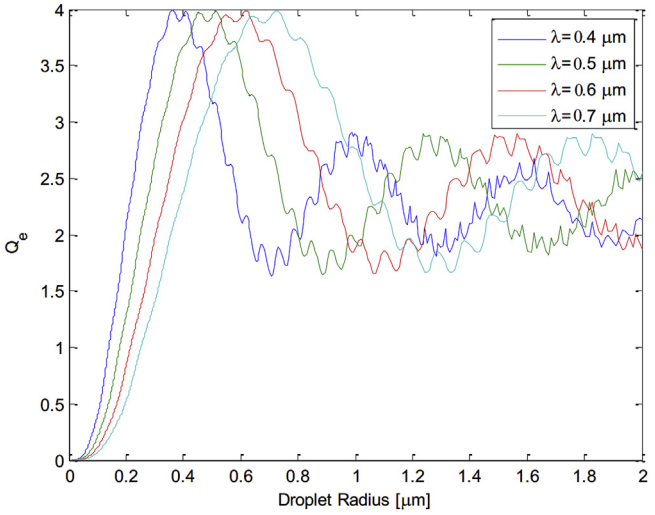

Fig. 1. The extinction efficiency for different wavelengths of light as a function of water droplet radius.

$$n(r) = \frac{n_{\text{total}}}{\sqrt{2\pi}\, r \ln \sigma_g} \exp\left[\frac{-\left(\ln \frac{r}{\bar{r}_g}\right)^2}{2(\ln \sigma_g)^2}\right] \tag{15}$$

where n_{total} is the total number of droplets per unit volume, $\bar{r}_g$ is the geometric mean radius and σ_g is the geometric standard deviation.

2.3. 2D boundary layer model

To properly describe superfog formation and its dispersion within the atmosphere, a two-dimensional boundary-layer based model is introduced. A simplified advection diffusion equation serves as the basis for the model. In this simplified form, the vertical component of velocity is considered to be negligible compared to the horizontal component of velocity ($v \ll u$). It is well justified for the environmental flows to consider only horizontal velocity, described by the logarithmic profile [27]. Also, at wind tunnel boundary layer conditions (high Reynolds number $Re = O(10^5)$), the thickness of boundary layer is smaller than the streamwise coordinate of boundary layer ($\delta \ll l$), therefore neglecting the horizontal diffusion term compared to the vertical diffusion term is reasonable ($\frac{\partial^2}{\partial x^2} \ll \frac{\partial^2}{\partial z^2}$).

$$\frac{\partial \phi}{\partial t} + u\frac{\partial \phi}{\partial x} = \frac{\partial}{\partial z} K_\phi \frac{\partial \phi}{\partial z} + S_\phi \tag{16}$$

where ϕ is a relevant transported property in 2D space, x is the downstream, horizontal, spatial coordinate, z is the vertical distance from the ground, $u(x,z)$ is the horizontal velocity of the air mass within the boundary-layer, t is time, K_ϕ and S_ϕ denote the eddy diffusivity and possible source term for property ϕ.. For eddy diffusivities of heat, vapor and liquid content, K_T, K_v, and $K_{C_{H_2O}}$, respectively, the following expressions have been used [28]:

$$K_T = \frac{0.35\, u_* z}{0.74 + 4.7\, \frac{z}{L}} \tag{17}$$

$$K_v = K_{C_{H_2O}} = \frac{0.35\, u_* z}{1 + 4.7 \frac{z}{L}} \tag{18}$$

Here u_* is the friction velocity, z is the vertical coordinate, and L is the Obukhov length. The crosswise and vertical components of velocity were neglected compared to streamwise component of velocity. A logarithmic wind profile is used for streamwise velocity as [29,30]:

$$u(z) = \frac{u_*}{\kappa}\left[\ln\left(\frac{z}{z_0}\right) + 4.7\, \frac{z}{L}\right] \tag{19}$$

Thus there is no need for a differential equation to compute u. In eq. (19), a roughness length of $z_0 = 0.01$ m was used to represent areas with low vegetation (e.g. grass and surface fuels under the forest canopy) [31,32]. The quantity κ is the Von Karman constant. Transport equations for temperature T, water vapor concentration v, and liquid water content C_{H2O}, are obtained by inserting T, v, and C_{H2O} for ϕ in eq. (16).

The source (sink) term, S_ϕ, in the case of the transported quantity $C_{H_2O}(v)$ is produced (consumed) through thermodynamic relations described via eqs. (1)–(11) applied to every grid point, thereby coupling the equilibrium thermodynamics model with the physics-based boundary layer equations. Other transported quantities do not have a source term. The necessary inputs for this model are: vapor flux and heat flux, surface temperature, relative humidity, friction velocity, Obukhov length, and roughness length.

The advection-diffusion equations are solved using an implicit finite difference method [33] expressed in terms of a generic transport variable as follows:

$$\frac{\varphi_{i,j}^{n+1} - \varphi_{i,j}^{n}}{\Delta t} + u_{i,j}\frac{\varphi_{i,j}^{n+1} - \varphi_{i-1,j}^{n+1}}{\Delta x} = \frac{2}{z_{j+1} - z_{j-1}}\left(k_{j+1/2}\frac{\varphi_{i,j+1}^{n+1} - \varphi_{i,j}^{n+1}}{z_{j+1} - z_j} - k_{j-1/2}\frac{\varphi_{i,j}^{n+1} - \varphi_{i,j-1}^{n+1}}{z_j - z_{j-1}}\right) \tag{20}$$

where the subscript i indicates the horizontal position of a grid point, subscript j indicates the vertical position of a grid point, superscript n indicates an iterative count.

The finite difference equation was further simplified:

$$\varphi_{i,j}^{n+1} - \varphi_{i,j}^{n} + \beta\left(\varphi_{i,j}^{n+1} - \varphi_{i-1,j}^{n+1}\right) = \alpha_{j+1/2}\left(\varphi_{i,j+1}^{n+1} - \varphi_{i,j}^{n+1}\right) - \alpha_{j-1/2}\left(\varphi_{i,j}^{n+1} - \varphi_{i,j-1}^{n+1}\right) \tag{21}$$

where the quantities α and β are defined as:

$$\beta = \frac{u_{i,j}\Delta t}{\Delta x} \tag{22}$$

$$\alpha_{j+1/2} = \frac{2k_{j+1/2}\Delta t}{(z_{j+1} - z_{j-1})(z_{j+1} - z_j)} \tag{23}$$

$$\alpha_{j-1/2} = \frac{2k_{j-1/2}\Delta t}{(z_{j+1} - z_{j-1})(z_j - z_{j-1})} \tag{24}$$

The simplified equations are solved using a tri-diagonal matrix solver. These equations were subject to the following boundary conditions for temperature, water vapor concentration, and liquid water content:

1. The first boundary condition is a zero flux for all three computed quantities, T, v and C_{H_2O}, at the top of the boundary-layer where the inversion layer prevents further transport in the vertical direction.

$$\frac{\partial T}{\partial z}(x, \delta) = 0, \quad \frac{\partial v}{\partial z}(x, \delta) = 0, \quad \frac{\partial C_{H_2O}}{\partial z}(x, \delta) = 0 \tag{25}$$

2. The second boundary condition is a constant flux of heat and vapor at the surface where smoldering fuels contribute. We assume that the heat and vapor flux is evenly distributed throughout the downwind distance at the surface of the model. In the case of C_{H_2O}, a zero-flux condition is imposed.

$$\frac{\partial T}{\partial z}(x, 0) = \frac{q''}{K_T}, \quad \frac{\partial v}{\partial z}(x, 0) = \frac{v''}{K_v}, \quad \frac{\partial C_{H_2O}}{\partial z}(x, 0) = 0 \tag{26}$$

Heat flux for the bottom boundary condition was approximated by calculating the temperature gradient from the measured temperatures. The water vapor produced from a smoldering fuel bed was approximated using stoichiometry.

The following boundary conditions are employed in the streamwise direction:

$$T(0, z) = T_{ambient}, \quad v(0, z) = 0, \quad C_{H_2o}(0, z) = C_{H_2o,\ ambient} \tag{27}$$

Fig. 2 shows a schematic of computational domain for 2D boundary layer model including boundary conditions and source terms.

2.4. Water vapor flux approximation

Assuming that wildland fuels can be described chemically as $C_6H_9O_4$ [34], the balanced complete combustion equation and thus maximum water vapor production:

$$4C_6H_9O_4 + 25O_2 + [0.322fmc \times H_2O + 94N_2] \rightarrow 18H_2O + 24CO_2 + [0.322fmc \times H_2O + 94N_2] \tag{28}$$

where *fmc* is the fuel moisture content (expressed as a percentage of the oven-dry mass of fuel). The compounds in brackets [ ] are present, but do not participate in the reaction. The mass of water vapor produced from combustion is approximated through stoichiometry to be

$$m_{H_2O,C_6H_9O_4} = 0.55 \times m_{C_6H_9O_4} \tag{29}$$

where $m_{H_2O,C_6H_9O_4}$ is the mass of water produced by combustion of hydrocarbon. The water vapor contributed from vaporization of water contained in moist fuels is calculated as follow:

$$m_{H_2O,vaporization} = m_{fuel}\frac{fmc}{1 + fmc} \tag{30}$$

where $m_{H_2O,vaporization}$ is the mass of water vapor contributed by vaporization. Assuming all fuel moisture evaporated, the water vapor produced from the combustion of the fuel bed can be expressed as

$$m_{H_2O,total} = m_{H_2O,C_6H_9O_4} + m_{H_2O,vaporization} \tag{31}$$

where $m_{H_2O,total}$ is the combined mass of water vapor produced from fuel bed.

3. Experimental methods

To provide data for and to evaluate specific aspects of our model, we designed three sets of experiments with hierarchically increasing complexity:

1. Thermodynamic Chamber Experiments: Mixing of cold and warm humid air masses
2. Boundary Layer Development Experiments: Air flow over smoldering fuel beds
3. Smoldering in Controlled Ambient

3.1. Thermodynamic Chamber Experiments

The superfog chamber was designed based on thermodynamic model described in Section 2 to simulate the interactions of two air masses with different temperatures and relative humidity through controlled mixing. During experiments, both the cool and warm air masses were pumped through separate ducts into the 60 cm × 60 cm × 90 cm superfog chamber for mixing (Fig. 3). The chamber was constructed of transparent acrylic material for visualization. Inlet aluminum ducts were 15.3 cm inner diameter with variable speed duct fans to force air masses into the chamber at the desired flow rates. The outlet duct was 20.3 cm in diameter. The cold air duct was cooled by liquid nitrogen forced through three 1.3 cm diameter copper coil heat exchangers. An electronic heater was used in the heated air duct. Two additional inlets were added to the heated duct for injection of water vapor from a humidifier and smoke particles (CCNs) from burning wooden sticks, leaves or paper. Omega Digital vane probe anemometers and Campbell Scientific HMP45C[1] temperature and relative humidity sensors were placed at each of the two inlet ducts and on the chamber exhaust. Temperature and relative humidity data were collected at 1 Hz and stored on a Campbell Scientific CR3000 data logger. As discussed in Section 2, the liquid water content and the visibility depend on both the number concentration and the size distribution of droplets. A TSI [35] Phase Doppler Particle Analyzer (PDPA) was used to measure the size distribution and number concentration of droplets formed through condensation in our test chamber.

3.2. Boundary Layer Development Experiments

A second set of experiments was conducted in a wind tunnel to validate the numerical 2D boundary layer model introduced in Section 2. The wind tunnel is located at the U.S. Forest Service PSW Research Station in Riverside, CA was originally designed to examine flame spread from a surface fuel into an elevated crown fuel [36,37]. The tunnel was modified to control temperature and humidity by adding refrigeration and water vapor production units [38]. In these experiments, we focused on the temperature profiles measured by thermocouples and video footage of smoke. Fig. 4(a) shows a simple schematic of our setup in the wind tunnel for the boundary layer experiments. The fuel beds composed of longleaf pine needles (*Pinus palustris* Mill.) were spread out evenly over the floor of the wind tunnel to a depth of 10–13 cm resulting in a fuel loading of 0.8 kg m^{-2}. Ten type K bare wire thermocouples located along the center line of the fuel bed immediately above the fuel bed from 76 to 265 cm every 21 cm downstream and four thermocouples deployed vertically 33, 52, 68, and 89 cm above the fuel bed at 181 cm downstream measured the horizontal and vertical temperature distribution (Fig. 4(b)). The exact location of thermocouples is tabulated in Table 1.

3.3. Smoldering in controlled ambient conditions

The third set of experiments consisted of burning baskets of longleaf pine needles under controlled ambient temperature, relative humidity and wind conditions. Visibility (V) was determined by measuring laser light transmission through the smoke [39]. As in Achtemeier [8], a Campbell Scientific HMP45C probe measured temperature and relative humidity. In the burning baskets sensible heat flux (Q_H) in the smoke was estimated with a Campbell Scientific CSAT3 sonic anemometer which measured temperature and vertical velocity fluctuations. Vertical total and radiative heat fluxes were measured with a Hukseflux RC01 sensor.

The goal of this experiment was to recreate conditions from known superfog events. Twenty-three possible parameter combinations relevant to documented superfog events were examined. Ambient temperature and relative humidity ranged from −1.1–15.6 °C and 60–95%, respectively. Table 2 summarizes different scenarios for smoldering in controlled ambient experiments. Highlighted combinations of temperature and humidity indicate conditions from actual superfog occurrences; blue highlights the 2008 I-4 Polk County event and yellow highlights conditions during the 2012 I-75 Gainesville event.

4. Results

First, we present theoretical model study based on equations

[1] The use of trade or firm names in this paper is for reader information and does not constitute endorsement by the U.S. Department of Agriculture of any product or service.

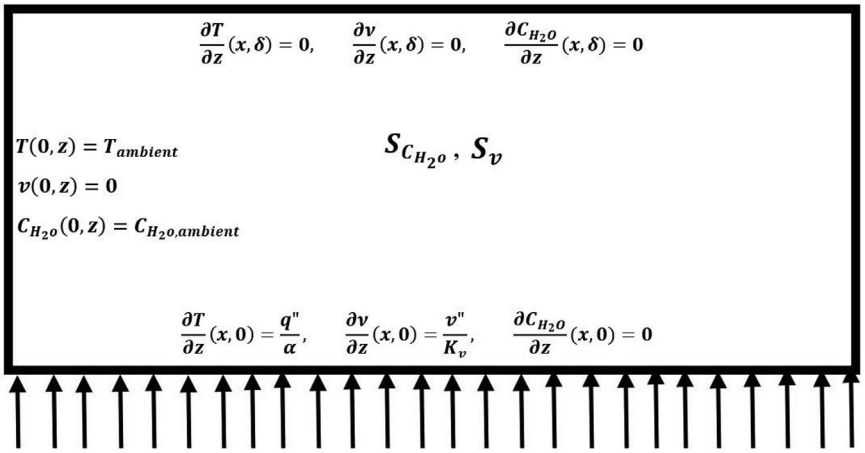

Fig. 2. Computational domain and boundary conditions for 2D boundary layer model.

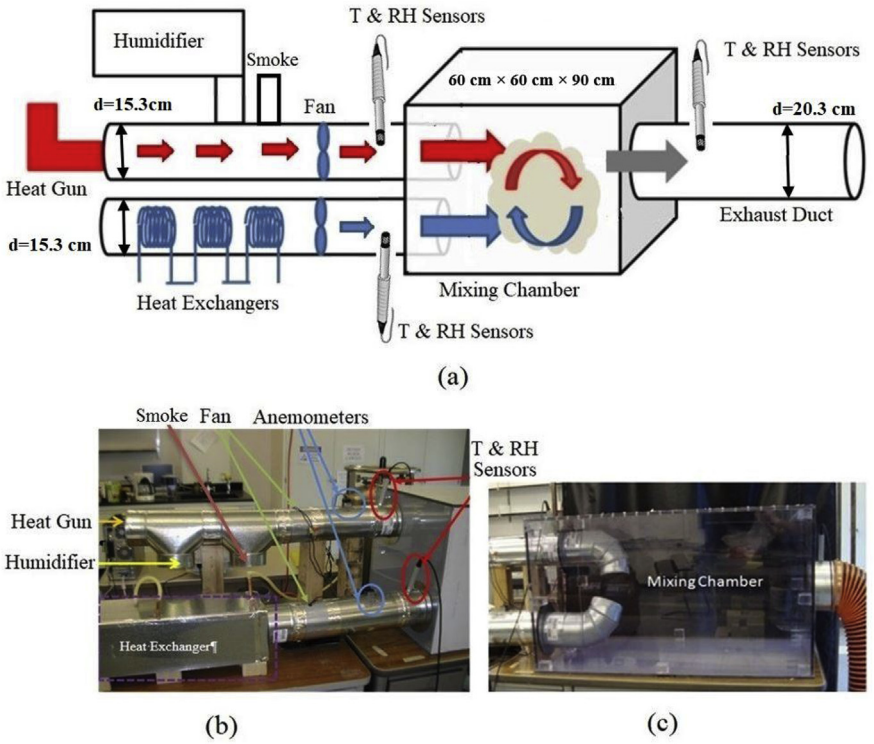

Fig. 3. Thermodynamic chamber experimental setup. Temperature (T), relative humidity (RH) and particle characteristic (PDPA) measurement locations indicated. (a): A schematic of setup. (b): A photograph of chamber inlets with instrument locations. (c): A photograph of optically clear acrylic chamber.

presented in Section 2. This model study enabled us to delineate parameter ranges of interest for possible visibility reductions to the superfog level. Next, we present experimental results from all three setups (Sections 4.2, 4.3, and 4.4). Application of the analysis to documented superfog events is found in Section 4.5.

4.1. Theoretical modeling

Achtemeier [7] measured temperature and relative humidity of residual smoldering combustion from prescribed fires and of ambient conditions. From these data, we estimated the final temperatures, mixing ratios, and liquid water contents when equal masses of smoke and ambient air are mixed (Table 3).

Based on these calculations from field data, estimated maximum available liquid water content (C_{H_2O}) was around 2 g m^{-3} which provides a limit on equations (1)–(11) by limiting the size distributions and number concentrations. With the known available liquid water content and desired visibility for superfog, a sensitivity study of the relationships between equations (1)–(11) was conducted. The effects of changing the geometric mean (r_g) and geometric standard deviation (σ_g) of the lognormal distribution of the droplet aerosols were investigated. Droplet size distributions with geometric mean radius between 1.0 and 10 μm and geometric standard deviations of σ_g = 1.3, 1.5 and 1.7 were used. Fig. 5(a) illustrates the relation between the liquid water content and the geometric mean radius for three iso-visibilities. In Fig. 5(a) and (b) the geometric standard deviation used was 1.8. Note that higher water content resulted in decreased visibility at a fixed particle size. For superfog visibility (3 m) Achtemeier [7] and known available liquid water content (2 g m^{-3}) the calculated geometric mean radius was ≤ 1 μm.

The modeled relationship between number density of droplet aerosols and mean geometric radius was also investigated (Fig. 5(b)) for

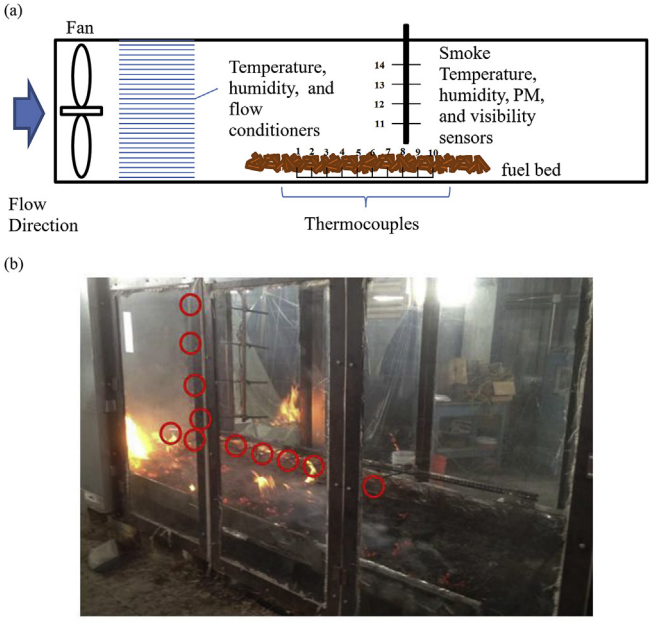

Fig. 4. (a)- Schematic of wind tunnel arrangement for boundary layer experiments. (b)- Photograph taken during a boundary layer experiment from the side of wind tunnel shows the smoldering fuel bed and thermocouple locations circled in red. (For interpretation of the references to colour in this figure legend, the reader is referred to the Web version of this article.)

Table 3
Calculation of liquid water content (C_{H_2O}) by the thermodynamic model using field data from Achtemeier [7].

T_{smoke} (°C)	w_{smoke} (g kg^{-1})	$T_{ambient}$ (°C)	$w_{ambient}$ (g kg^{-1})	T_{final} (°C)	w_3 (g kg^{-1})	w_{sat} (g kg^{-1})	C_{H_2O} (g m^{-3})
42.1	52.0	15	6.2	29.9	29.1	28.8	0.39
41.2	47.2	15	6.2	28.7	26.7	26.7	0.03
46.4	61.7	15	6.2	32.6	33.9	33.5	0.47
40.3	46.7	15	6.2	28.4	26.5	26.3	0.15
54.1	93.9	15	6.2	38.9	50.1	48.9	1.36
45.8	60.1	15	6.2	32.1	33.2	32.8	0.44
62.5	134.3	15	6.2	44.9	70.3	68.7	1.70

droplet distributions centered about 6 μm or greater, the number of droplets formed seemed insensitive to σ_g (Fig. 5(d)). However, at smaller sizes the number density necessary for superfog formation played a greater role. For viable liquid water content values and distributions with mean geometric radius less than 1 μm, the size distribution standard deviation may not be larger than 1.3 to achieve the number density required for superfog visibility (around $n = 10^5$ # cm^{-3}).

4.2. Thermodynamic chamber results

Results from the thermodynamic chamber experiment described in Section 3.2 are analyzed in detail. Table 4 lists different characteristics of air masses including the temperature, relative humidity, water content, droplet concentration, and visibility for each experiment. The experiments compared two cases of mixing warm and cool air masses. In the first case a warm air mass of 32.2 °C and 96.1% relative humidity mixed with a cooler air mass of 8.1 °C and 99.1% relative humidity. In the second case a warm air mass of 27.0 °C and 61.8% humidity was combined with a cooler air mass of 11.1 °C and 98.1% humidity. Five repetitions were made for each experimental setting.

Table 1
Location of thermocouples. Downwind position is measured from the leading edge of the fuel bed and the vertical position is measured from the base of the fuel bed. See Fig. 4 for schematic.

Thermocouple number	1	2	3	4	5	6	7	8	9	10	11	12	13	14
Downwind position (cm)	75	97	119	139	163	181	202	218	239	260	181	181	181	181
Vertical position (cm)	13	13	13	13	13	13	13	13	13	13	33	52	68	89

Table 2
Summary of smoldering in controlled ambient experiments. Experiments are named as 'E' followed by the experiment number. Highlighted combinations of temperature and humidity indicate conditions from the actual Superfog occurrences. Blue highlighted cells represent conditions during the I-4 disaster in 2008. Yellow highlighted areas represent conditions during the Gainesville incident in 2012.

	T (°C)						
RH %	-1.1	1.7	4.4	7.2	10	12.8	15.6
60							
65			E3	E9			
70				E10		E19	E22
75			E4	E11	E15	E20	E23
80			E5	E12	E16	E21	
85			E6		E17		
90			E7	E13			
95	E1	E2	E8	E14	E18		

Results from the chamber study indicated that it was possible to generate low visibility fog without the presence of smoldering combustion. The initial set of experiments consisted of taking pictures of fog formation events within the chamber using a digital camera under various inlet conditions. Fig. 6(a) provides a base visibility and depth of vision prior to the fog formation experiment. An image taken during a fog formation experiment is given in Fig. 6(b). It is evident in this photograph that the background cabinets and labeling are no longer visible. The chair which is 120 cm away from the chamber can barely be seen. The top, warm air, duct is barely visible although it is only 45 cm from the front side of the chamber.

This type of simple visualization provided a reliable qualitative measure of fog formation based on the decrease of visibility, but quantitative results were needed for model validation. Based on the relationships between droplet size distribution and number concentrations from Section 2 we developed a method to approximate the visibility distance that required a particle size distribution within the chamber as an input. We measured the droplet size distribution and number concentration of fog formed within the mixing chamber with a TSI Phase Doppler Particle Analyzer (PDPA) (Fig. 7). The averaged number of droplets, over five repetitions, are $n_{total} = 18807$ and

different visibilities. For the same droplet distribution with a geometric radius of 1 μm or less, the number density of particles for the fog should be of the order of 10^5 # cm^{-3} or greater. For superfog visibility (3 m), the influence of geometric standard deviation on required liquid water content and number density was investigated. As the variability in the distribution increased, higher liquid water was required in order to achieve superfog visibility at a given mean diameter. The liquid water content required for superfog was most sensitive to particle size when the standard deviation was lowest. For a particular visibility, any increases to either the mean geometric size or geometric standard deviation lead to increases in liquid water content needed (Fig. 5(c)). For

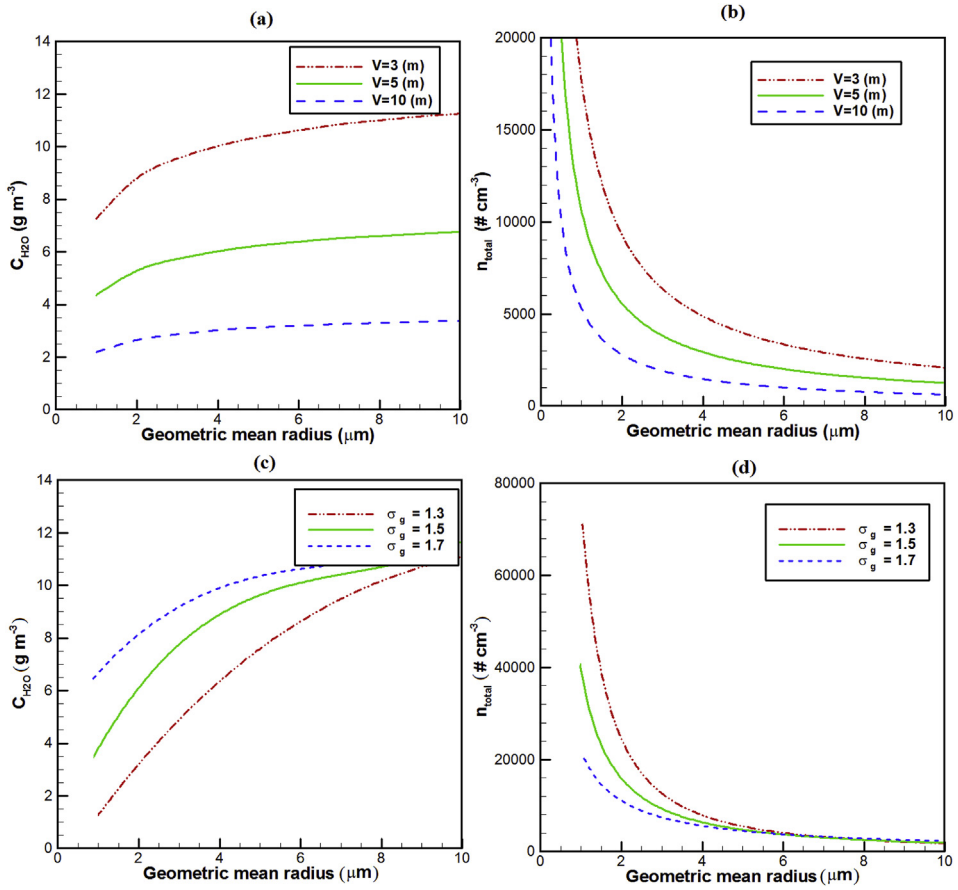

Fig. 5. Modelled relationships between liquid water content C_{H_2O}, geometric mean radius $\bar{r}_g$, geometric standard deviation σ_g and visibility V.

Table 4
Characteristics of air masses mixed in chamber experiment to produce fog.

Warm		Cold		Mixture				
T (°C)	RH%	T (°C)	RH%	T (°C)	RH%	C_{H_2O}(g m^{-3})	n_{total}(# cm^{-3})	V (m)
32.2	96.1	8.1	99.1	17.9	> 100	5.5	49000	3.5
27.0	61.8	11.1	98.1	14.9	> 100	2.0	20000	4.5

n_{total} = 17256 for case 1 and case 2, respectively.

The mode of the measured distribution is in the range between 1 and 2 μm (Fig. 7). The experiments resemble a lognormal distribution with mean radius of 1.5 μm, and standard deviations of σ = 1.4 and 1.6. The larger droplets can greatly reduce visibility but greatly increase liquid water content needed.

Relative humidity of both mixtures exceeded 100% indicating fog formation (Table 4). In the both cases, the liquid water content reached and exceeded 2.0 g m^{-3} and the calculated visibility V was close to superfog levels. Larger droplets can also greatly reduce visibility, but the required liquid water content increases dramatically.

4.3. Boundary layer results

This section analyzes the results of the boundary layer development experiment described in Section 3.2. The sensible heat flux Q_H, produced by smoldering ranged from an initial maximum of 3.5 to a minimum of 1 kW m^{-2} before smoldering combustion ceased (Table 5). For the 400 g of pine needles, water vapor production was estimated using eqs. (29)–(31). The pine needles were soaked in water up to 5 min

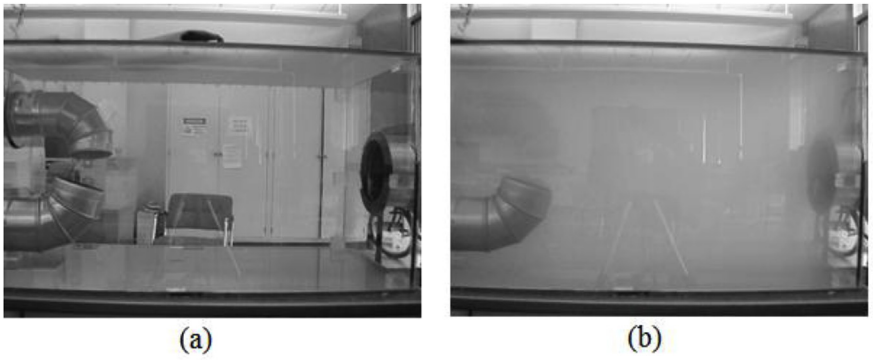

Fig. 6. Example of visibility reduction due to mixing of hot and cold moist air masses without presence of smoke.

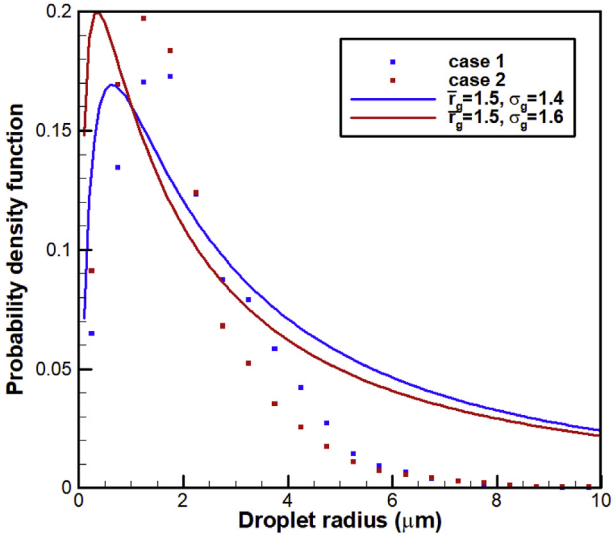

Fig. 7. Average droplet size distribution measured from the fog test chamber experiments (case 1 and 2), the fit lognormal distributions ($\bar{r}_g = 1.5\,\mu m$, $\sigma_g = 1.4\,\mu m$) and ($\bar{r}_g = 1.5\,\mu m$, $\sigma_g = 1.6\,\mu m$).

Table 5
Fuel moisture content, temperature, humidity, and maximum sensible heat (Q_H) for smoldering longleaf pine needle fuel beds.

Experiment #	**M** (%)	T (°C)	RH (%)	$\mathbf{Q_H}$ (**kW m**$^{-2}$)
1	9.0	26.6	35	_
2	36.0	13.4	52	2.3
3	36.8	12.8	52	1.1
4	39.0	15.3	52	3.1
5	40.4	11.8	45	3.2
6	41.6	13.5	34	2.8
7	43.3	12.8	45	3.4
8	43.3	12.5	30	3.5

before ignition to achieve these high levels of moisture content for dead fuels [40]. This fuel mass could produce 220–310 g of water vapor for moisture content. The needles typically smoldered for 30 min resulting in an estimated water vapor flux of 1.6–2.4 g m^{-2} s^{-1}.

It was difficult to replicate superfog formation conditions in the wind tunnel with the spread fuel bed configuration used in the boundary layer growth experiment because the availability of oxygen caused most of combustion to occur in the flaming phase leaving little for the smoldering phase. For this reason, to compare the model results with the experiments we focused on the fog conditions corresponding to liquid water content of 0.1 g kg^{-1}. This liquid water content corresponds to a visible formation of smoke but not as visually impeding as superfog that must have at least 2.0 g kg^{-1} of liquid water content. However, this value was good enough to validate the model. Table 6 summarizes the experimental parameters that were used as model inputs for validation. Fig. 8 presents predicted vs observed boundary layer height. For larger distances along the fuel bed, the model under predicts the depth of the boundary layer.

4.4. Smoldering in controlled ambient conditions

This section provides the results of smoldering from the controlled ambient experiment (section 3.3, Table 2). Climate conditions corresponding to I-4 and I-75 events are indicated in Table 2. The measured values for smoke humidity, temperature, and visibility are provided in Tables 7–9, respectively. Downwind temperature sensors indicated that smoke temperature was consistently 3–8 °C higher than ambient conditions throughout the experiments. Although we were not able to

Table 6
Model Inputs for numerical boundary layer model.

Symbol	Parameter	Value
v''	Vapor flux	1.6 × g m^{-2} s^{-1}
q''	Heat flux	1.0 kW m^{-2}
u_*	Friction velocity	0.1 m s^{-1}
L	Obukhov length	100 m
z_0	Roughness height	0.01 m
T_s	Surface air temperature	12 °C
$\frac{\partial T}{\partial z}$	Vertical temperature gradient	24 °C m^{-1}
$RH_{ambient}$	Ambient relative humidity	45%

Note: friction velocity is obtained as the best fit of logarithmic profile (equation (19)) to the measured velocities within the wind tunnel.

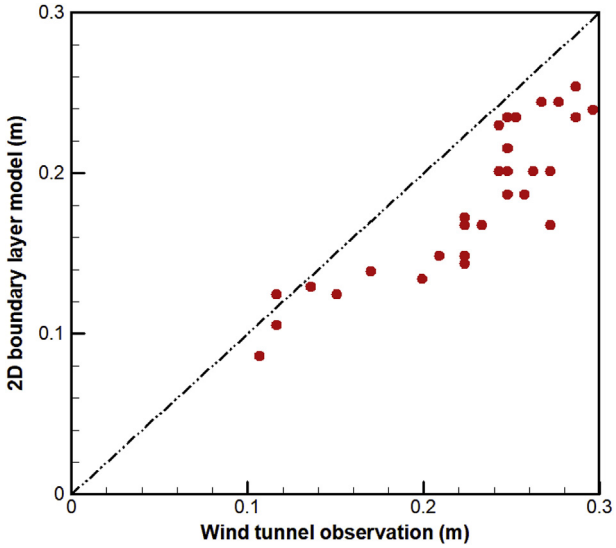

Fig. 8. Comparison of smog boundary layer height between 2D boundary layer model prediction and wind tunnel observation for the fog condition corresponding to liquid water content of 0.1 g kg^{-1}.

Table 7
Summary of averaged smoke humidity measurements (%).

RH %	T (°C)						
	−1.1	1.7	4.4	7.2	10	12.8	15.6
60							
65			70	41			
70				40			23.5
75			65	40	40		40
80			60	40		50	
85			70		60		
90			107	80			
95	100	100	100	44	44		

cover all documented ranges, it was possible to create low visibility conditions in the wind tunnel under a range of ambient temperature and relative humidity. As Fig. 9 shows, increasing fuel moisture content M caused a dramatic difference in the fog thickness under constant temperature and humidity. While M ranged from 7 to over 40% in the experiments, superfog visibilities were generally associated with M of 30–50%.

4.5. Analysis of documented I-4 and I-75 superfog events

After obtaining key inputs from smoke measurements and validating the boundary layer growth model, the model was deployed to

Table 8
Summary of averaged smoke temperatures (°C).

RH %	T (°C)						
	−1.1	1.7	4.4	7.2	10	12.8	15.6
60							
65			12	15			
70				16			21
75			10	20	16		24
80			16.7	16		19.5	
85			14		16		
90			8	12			
95	5	5	10	16	16		

Table 9
Summary of averaged visibility measurements (m).

RH %	T (°C)						
	−1.1	1.7	4.4	7.2	10	12.8	15.6
60							
65			0.29	0.29			
70				0.27			0.84
75			0.29	3.44	1.27		0.38
80			3.44	1.27			
85			1.28		1.24		
90			0.62	0.26			
95	0.37	0.29	0.59	0.67	0.67		

predict the occurrence of superfog for the I-4 event and the I-75 events. A summary of the model input values used for the boundary layer model is presented in Table 10. The model predicted the boundary layer depth as a function of downwind distance from the smoke source. The simulation results are presented in Fig. 10(a) and (b) for I-4 and I-75 events, respectively. The green dash dot curve represents a smoothed polynomial fit to the model output. Based on the criterion $C_{H2O} > 2.0\,g\,m^{-3}$ for superfog visibility, the thermodynamic model predicted that superfog formed at a depth of 1 m within 30 m of the smoke source. A statistical fit of the model output in the form $h = cx^{0.5}$ fit the simulated data well. Here h is the boundary layer depth, x is the distance along the smoldering bed and c is a constant. The best fit to I-4 and I-75 data yielded $c = 0.175$ and $c = 0.2$, respectively.

5. Summary

Thermodynamic equilibrium modeling has allowed us to estimate fog formation or the lack of fog formation through mixing of air masses with different temperature and moisture contents. A potential limit for the liquid water content C_{H_2O} values ($2\,g\,m^{-3}$) available from smoldering smoke to produce superfog was obtained based on the published experimental data by Achtemeier [7]. A theoretical sensitivity analysis was performed to determine the relationships between liquid water content, droplet size distribution and visibility. If the available liquid water content is limited to $2\,g\,m^{-3}$, then droplets need to have a radius of 1 μm or smaller to reduce visibility to superfog levels. Droplet distributions with geometric standard deviations greater than 1.3 lead to the inclusion of large droplets. These larger droplets have lower extinction efficiency and require more liquid water. Droplet concentrations of around 10^5 # cm^{-3} are required to form superfog which is typically exceeded in biomass burns.

To explore the influence of turbulent mixing, advection and surface fluxes a two-dimensional boundary-layer model that includes thermodynamic processes to model condensation of water vapor to form fog was formulated. Experiments were conducted to measure key parameters associated with smoldering smokes. Controlled superfog experiments showed the ability to form superfog in the wind tunnel under various temperature, humidity and fuel moisture content combinations. Superfog in these experiments have appeared when ambient temperatures are less than 4 °C, the humidity is over 80%, and fuel moisture content values are 40% or greater. It has been shown through experiments that the fuel moisture content plays a crucial role in the quality of superfog produced. The high fuel moisture content allows more water vapor to be included into the smoke through vaporization. Boundary-layer growth predictions from the 2D physics-based model were verified with experiments. The model was able to predict conditions matching historic superfog events on the I-4 in 2008 and the I-75 in 2012.

Conflicts of interest

This manuscript does not contain any proprietary information nor information that may lead to any conflicts of interest. Comprehensive experimental and numerical studies of the superfog formation from wildland fires have been carried out. This manuscript is solely under consideration for publishing in the Fire Safety Journal.

Acknowledgements

This work was supported by the USDA Joint Fire Science Program project 09-1-04-5 administered by USDA Forest Service PSW Research Station agreement 09-JV-11272166-049. The authors gratefully acknowledge the assistance provided by several University of California, Riverside students: Hector Gonzalez, Kevin Tsui, Victor Lu, Godiva Kam, Jitmohan Lalay, Kurtis Watanabe, Mitchell Shinn, Stephen Coffer, George Knight, Annemarie Fata, Manuel Michael, and Danny Huerta. We are also appreciative for the technical assistance provided by Joey Chong and Gary Achtemeier of the U.S. Forest Service.

Fig. 9. (a) Light smoke formed under ambient temperature of 5 °C, 76% relative humidity, and 7% fuel moisture content. (b) superfog formed under ambient temperature of 6 °C, 88% relative humidity, and 40% fuel moisture content.

Table 10
Model Inputs for documented I-4 and I-75 superfog incidents.

Symbol	Parameter	Value
v''	Vapor flux	$1.6 \times$ g m^{-2} s^{-1}
q''	Heat flux	1.0 kW m^{-2}
u_*	Friction velocity	0.1 m s^{-1}
L	Obukhov length	100 m
z_0	Roughness height	0.01 m
T_s	Surface air temperature	1.66 °C (I– 75 Gainesville 2012)10 °C (I– 4 Polk County 2008)
$\frac{\partial T}{\partial z}$	Vertical temperature gradient	3 °C km^{-1}
RH_{ambient}	Ambient relative humidity	90% (I– 75) 85 % (I– 4)

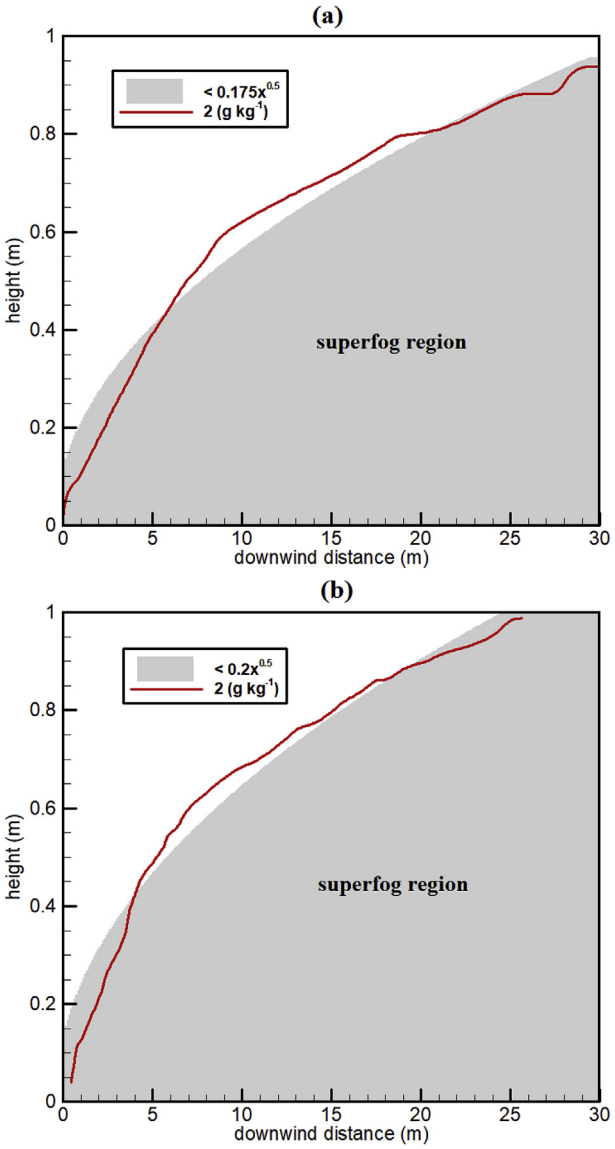

Fig. 10. Boundary-layer model prediction of growth of superfog using weather conditions surrounding the (a) I-4 event in 2008 and the (b) I-75 event in 2012. Superfog is defined to be anywhere where liquid water content is greater than 2.0 g m^{-3}. Over the course of 30 m, superfog grows to a height of 1 m.

References

[1] T.A. Waldrop, S.L. Goodrick, Introduction to Prescribed Fires in Southern Ecosystems, USDA Forest Service, Southern Research Station, Asheville, NC, 2012.

[2] M.A. Melvin, National Prescribed Fire Use Survey Report. Technical Report 02–15, Coalition of Prescribed Fire Councils, Inc., 2015, https://docs.google.com/a/prescribedfire.net/viewer?a=v&pid=sites&srcid=cHJlc2NyaWJlZGZpcmUubmV0fGNvYWxpdGlvbi1vZi1wcmVzY3JpYmVkLWZpcmUtY291bmNpbHN8Z3g6NWY5NTQ5ZDg3ODVmYTBhMw%5Cnhttp://www.prescribedfire.net/ 2015.

[3] H.E. Mobley, Southern Forestry Smoke Management Guidebook, USDA Forest Service, Southeastern Forest Experiment Station, Asheville, NC, 1976.

[4] G.L. Achtemeier, Simulating nocturnal smoke movement, Fire Manag. Today. 61 (2001) 28–33.

[5] G.L. Achtemeier, On the origins of "superfog" - a combination of smoke and water vapor that produces zero visibility over roadways, Second Int. Wildl. Fire Ecol. Fire Manag. Congr. Fifth Symp. Fire for. Meteorol., Orlando, Florida, 2003, pp. 1–4.

[6] G.L. Achtemeier, Effects of moisture released during forest burning on fog formation and, J. Appl. Meteorol. Climatol. 47 (2008) 1287–1296, https://doi.org/10.1175/2007JAMC1721.1.

[7] G. Achtemeier, On the formation of superfog in woodland smoke, Meteorol. Appl. 16 (2009) 215–225.

[8] G.L. Achtemeier, Measurements of moisture in smoldering smoke and implications for fog, Int. J. Wildland Fire 15 (2006) 517, https://doi.org/10.1071/WF05115.

[9] J. Aurell, B.K. Gullett, Emission factors from aerial and ground measurements of field and laboratory forest burns in the southeastern U.S.: PM $_{2.5}$, black and brown carbon, VOC, and PCDD/PCDF, Environ. Sci. Technol. (2013), https://doi.org/10.1021/es402101k 130729092352005.

[10] I. Bertschi, R.J. Yokelson, D.E. Ward, R.E. Babbitt, R.A. Susott, J.G. Goode, W.M. Hao, Trace gas and particle emissions from fires in large diameter and belowground biomass fuels, J. Geophys. Res. 108 (2003) 8472.

[11] C. Geron, M. Hays, Air emissions from organic soil burning on the coastal plain of North Carolina, Atmos. Environ. 64 (2013) 192–199, https://doi.org/10.1016/j.atmosenv.2012.09.065.

[12] P.G. Duynkerke, Radiation fog: a comparison of model simulation with detailed observations, Mon. Weather Rev. 119 (1990) 324–341.

[13] M. Nakanishi, H. Niino, An improved mellor-yamada level-3 model: its numerical stability and application to a regional prediction of advection fog, Boundary-Layer Meteorol. 119 (2006) 397–407, https://doi.org/10.1007/s10546-005-9030-8.

[14] R. Nebuloni, Empirical relationships between extinction coefficient and visibility in fog, Appl. Opt. 44 (2005) 3795–3804.

[15] M. Kumai, formation of ice crystals and dissipation of supercooled fog by artificial nucleation and variations of crystal habit at early growth stages, J. Appl. Meteorol. 21 (1981) 579–589.

[16] M. Farzaneh, O. Melo, Properties and effect of freezing rain and winter fog on outline insulators, Cold Reg. Sci. Technol. 19 (1990) 33–46.

[17] E.L. Currier, J.B. Knox, T. V Crawford, E.L. Currier, J.B. Knox, T.V.C. Cooling, E.L. Currier, J.B. Knox, T.V. Crawford, Cooling pond steam fog, J. Air Pollut. Control Assoc. 24 (1974) 860–864, https://doi.org/10.1080/00022470.1974.10469983.

[18] R.B. Stull, An Introduction to Boundary Layer Meteorology, (1988), https://doi.org/10.1007/978-94-009-3027-8.

[19] P.R. Lowe, An approximating polynomial for the computation of saturation vapor pressure, J. Appl. Meteorol. 16 (1977) 100–103.

[20] P. Chylek, Extinction of liquid water content of fogs and clouds, J. Atmos. Sci. 35 (1977) 296–300.

[21] I.N. Tang, Chemical and size effects of hygroscopic aerosols on light scattering coefficients, J. Geophys. Res. 101 (1996) 19245–19250.

[22] B.A. Kunkel, Parameterization of droplet terminal velocity and extinction coefficient in fog models, J. Clim. Appl. Meteorol. 23 (1984) 34–41, https://doi.org/10.1175/1520-0450(1984)023<0034:PODTVA>2.0.CO;2.

[23] W.C. Hinds, Aerosol Technology: Properties, Behavior, and Measurement of Airborne Particles, second ed., (1999).

[24] S.K. Friedlander, Smoke, Dust, and Haze: Fundamentals of Aerosol Dynamics, Oxford University Press, 2000.

[25] J. Aitchison, J.A.C. Brown, The Lognormal Distribution, with Special Reference to its Uses in Economics, Cambridge Univ. Press., London, 1957.

[26] J. Podzimek, Droplet concentration and size distribution in haze and fog, Studia Geophys. Geod. 41 (1997) 277–296.

[27] P. Richards, R. Hoxey, Appropriate boundary conditions for computational wind engineering models using the k–e turbulence mode, J. Wind Eng. Ind. Aerod. 46–47 (1993) 145–153.

[28] F.T.M. Nieuwstadt, P. Van Ulden, A numerical study on the vertical dispersion of passive contaminants from a continuous source in the atmospheric surface layer, Atmos. Environ. 12 (1978) 2119–2124.
[29] F.A. Albini, R.G. Baughman, Estimating Windspeeds for Predicting Wildland Fire Behavior, Res. Pap. INT-221. Ogden, UT USDA For. Serv. Intermt. For. Range Exp. Station, 1979.
[30] A. Cimorelli, S. Perry, A. Venkatram, J. Weil, R. Paine, R. Wilson, R. Lee, W. Peters, R. Brode, AERMOD : a dispersion model for industrial source applications . Part I : general model Formulation and boundary layer characterization, J. Appl. Meteorol. 44 (2005) 682–693.
[31] G. Stanhill, A simple instrument for the field measurement of turbulent diffusion flux, J. Appl. Meteorol. 8 (1969) 509–513 https://doi.org/10.1016/B978-012386660-8/50006-4.
[32] B. Blocken, Computational Fluid Dynamics for urban physics: importance, scales, possibilities, limitations and ten tips and tricks towards accurate and reliable simulations, Build. Environ. 91 (2015) 219–245, https://doi.org/10.1016/j.buildenv.2015.02.015.
[33] M.M. Meerschaert, C. Tadjeran, Finite difference approximations for fractional advection-dispersion flow equations, J. Comput. Appl. Math. 172 (2004) 65–77, https://doi.org/10.1016/j.cam.2004.01.033.
[34] G.M. Byram, Combustion of forest fuels, in: K.P. Davis (Ed.), Forest Fire: Control and Use. McGraw-Hill, New York, 1959.
[35] W.D. Bachalo, The phase Doppler Method : analysis , performance evaluations , and applications, part, Part. Syst. Charact. 11 (1994) 73–83.
[36] J.S. Lozano, An Investigation of Surface and Crown Fire Dynamics in Shrub Fuels, Dissertation, University of California, 2011.
[37] W. Tachajapong, J. Lozano, S. Mahalingam, X. Zhou, D.R. Weise, Experimental and Numerical Modeling of Shrub Crown Fire Initiation, (2009), pp. 618–640.
[38] M. Princevac, D. Weise, A. Venkatram, G. Achtemeier, S. Mahalingam, S. Goodrick, C. Bartolome, Superfog Formation: Laboratory Experiments and Model Development, University of California - Riverside, Riverside, CA, 2013.
[39] C.J. Bartolome, Formation of Superfog from Wildland Fires: Theoretical and Physical Modeling, University of California, Riverside, 2014.
[40] R.M. Nelson, Water relations of forest fuels, For. Fires Behav. Ecol. Eff, Academic Press, San Diego, CA, 2001, pp. 79–149.